



# **Ship-based estimates of momentum transfer coefficient over sea ice and recommendations for its parameterization**

Piyush Srivastava<sup>1,5</sup>, Ian M. Brooks<sup>1</sup>, John Prytherch<sup>2,6</sup>, Dominic J. Salisbury<sup>1</sup>, Andrew D.  
Elvidge<sup>3</sup>, Ian A. Renfrew<sup>3</sup> and Margaret J. Yelland<sup>4</sup>

<sup>1</sup>School of Earth & Environment, University of Leeds, Leeds, LS2 9JT, UK

<sup>2</sup>Department of Meteorology, University of Stockholm, Stockholm, Sweden

<sup>3</sup>School of Environmental Sciences, University of East Anglia, Norwich, UK

<sup>4</sup>National Oceanography Centre, Southampton, UK

<sup>5</sup>Centre of Excellence in Disaster and Mitigation and Management, Indian Institute of  
Technology, Roorkee, India

<sup>6</sup>Bolin Centre for Climate Research, University of Stockholm, Stockholm, Sweden

Corresponding author: Piyush Srivastava ([p.srivastava@leeds.ac.uk](mailto:p.srivastava@leeds.ac.uk))



19

## 20 **Abstract**

21

22 A major source of uncertainty in both climate projections and seasonal forecasting of sea ice is  
23 inadequate representation of surface–atmosphere exchange processes. The observations needed to  
24 improve understanding and reduce uncertainty in surface exchange parameterizations are challenging  
25 to make and rare. Here we present a large dataset of ship-based measurements of surface momentum  
26 exchange (surface drag) in the vicinity of sea ice from the Arctic Clouds in Summer Experiment  
27 (ACSE) in July–October 2014, and the Arctic Ocean 2016 experiment (AO2016) in August–September  
28 2016. The combined dataset provides an extensive record of momentum flux over a wide range of  
29 surface conditions spanning the late summer melt and early autumn freeze-up periods, and a wide  
30 range of atmospheric stabilities. Surface exchange coefficients are estimated from in situ eddy  
31 covariance measurements. The local sea-ice fraction is determined via automated processing of  
32 imagery from ship-mounted cameras. The surface drag coefficient,  $C_{D10n}$ , peaks at local ice fractions  
33 of 0.6–0.8, consistent with both recent aircraft-based observations and theory. Two state-of-the-art  
34 parameterizations have been tuned to our observations with both providing excellent fits to the  
35 measurements.

36



## 1 Introduction

The Arctic region is changing rapidly. Surface temperatures are rising at a rate more than twice the planetary average, a process known as Arctic Amplification (Serreze and Barry, 2011; Cohen et al., 2014; Stuecker et al., 2018; Dai et al., 2019). Such rapid warming is drastically altering the physical landscape of the Arctic, most visibly the dramatic reduction in sea-ice extent (Onarheim et al., 2018), thickness, and age (Ricker et al., 2017; Kwok, 2018), and has the potential to impact a host of biological and chemical processes (Howes et al., 2015; Lehnher et al., 2018). Changes in the Arctic may also impact lower latitudes via modification of weather patterns and ocean circulation (Cohen et al., 2014; Overland et al., 2016).

Whilst climate models robustly reproduce Arctic amplification, they have been less successful in making accurate seasonal forecasts of sea-ice extent (Stroeve et al., 2014) or even capturing the observed sea ice decline over the past decades (Stroeve et al., 2012). There is also large inter-model variability in projections of future climate over varying timescales (Hodson et al., 2013; Stroeve et al., 2014; Zampieri et al., 2018). A major source of uncertainty in models is the representation of turbulence-driven surface exchanges (Bourassa et al., 2013; Vihma et al., 2014; Tsamados et al., 2014; LeMone et al., 2018). Turbulent exchange is a subgrid-scale process parameterized in terms of resolved model variables and surface transfer coefficients. A lack of observational data in high-latitude environments has resulted in large uncertainty in the parameterization of the transfer coefficients of momentum ( $C_D$ ), heat ( $C_H$ ) and moisture ( $C_E$ ). Here, we focus on the parameterization of the momentum transfer (drag) coefficient,  $C_D$ .

The exchange of momentum between the atmosphere and sea ice directly affects the dynamical evolution of both the atmospheric boundary layer and the sea ice. The exchange is partly dependent on physical properties of the surface. With ongoing sea ice loss and the increasing spatial extent of the Arctic Ocean's marginal ice zone (MIZ) (Strong and Rigor, 2013; Rolph et al., 2020), the nature of this exchange is subject to change, implying improved understanding of the physical processes is critical. Recent studies have shown that the model reproduction of future sea-ice thickness and extent (Rae et al., 2014; Tsamados et al., 2014), the near-surface atmosphere (Rae et al., 2014; Renfrew et al., 2019), and the polar ocean (Stoessel et al., 2008; Roy et al., 2015) are all sensitive to the parameterization of surface momentum exchange over sea ice.

Most models have rather simplified approaches for parameterizing the transfer coefficients over sea ice: prescribing either a constant value for equivalent neutral transfer coefficients for all sea ice, or two



different values, corresponding to the MIZ and pack ice conditions along with empirical ice morphological parameters (Notz, 2012; Lüpkes et al., 2013; Elvidge et al., 2016). They then typically utilize a classical ‘mosaic’ or ‘flux averaging’ approach where fluxes are estimated separately over sea ice and open water for each grid box and an ‘effective’ turbulent flux is calculated as the weighted average using the fractions of open water and sea ice (Claussen, 1990; Vihma, 1995).

For models that assume a fixed  $C_{D10n}$  over ice, the flux averaging method leads to a monotonically increasing  $C_{D10n}$  across the MIZ; this is not supported by observations (Mai et al., 1996; Hartman et al., 1994; Schroder et al., 2003; Andreas et al., 2010; Elvidge et al., 2016) which indicate a peak at ice fractions of 50-80%. The value of sea-ice concentration at which  $C_{D10n}$  peaks depends upon the ice-morphology (Elvidge et al., 2016). It arises due to the contribution of form drag at the edges of floes, leads, melt ponds and ridges (Arya 1973, 1975; Andreas et al., 2010; Lüpkes et al., 2012, Lüpkes and Gryanik, 2015; Elvidge et al., 2016).

Andreas et al. (2010) suggested a simple empirically-based parameterization of  $C_{D10n}$  in terms of a quadratic function of ice concentration. Based on theoretical considerations (Arya, 1973; Arya, 1975; Hanssen-Bauer and Gjessing, 1988; Garbrecht et al., 2002; Birnbaum and Lüpkes, 2002; Lüpkes and Birnbaum, 2005), Lüpkes et al. (2012; L2012 hereafter) developed a physically-based hierarchical parameterization for  $C_{D10n}$  which, in its lowest level of complexity, requires only ice fraction as the independent variable. The L2012 parameterization scheme qualitatively reproduces the observed peak in  $C_{D10n}$  over the MIZ.

Recently, Elvidge et al. (2016; E2016) used aircraft measurements over the Arctic MIZ to develop a data set of 195 independent estimates of  $C_{D10n}$  over the MIZ, more than doubling the number of observations previously available. Their observations were consistent with the theory of L2012; however, they found a large variation in  $C_{D10ni}$  ( $C_{D10n}$  for 100% ice cover) demonstrating that this depends strongly on ice morphology – as also found by Castellani et al. (2014) who applied bulk parameterizations to ice morphology data based on laser altimetry. E2016 recommended modified values of key parameters in the L2012 scheme and, subsequently, this scheme with these settings has been implemented in the Met Office Unified Model (MetUM). Renfrew et al. (2019) demonstrated that this new scheme significantly reduced biases and root-mean-square errors in the simulated wind speed, air temperature and momentum flux over, and downstream of, the MIZ; in addition to having widespread impacts throughout the Arctic and Antarctic via, e.g., mean sea level pressure. The new scheme became part of the operational forecasting system at the Met Office in September 2018 and



99 part of the latest climate model configuration (in GL8). However, at present a constant value of  $C_{D10ni}$   
 100 is used; a known limitation in the veracity of surface momentum exchange over sea ice.

101 At present, the complexity of physically-based parameterizations of momentum exchange over sea ice  
 102 exceeds the parameterization constraints provided by observations. In other words, despite recent  
 103 progress, we are still lacking the observational data sets required for further parameterization  
 104 development. Here, we utilize a large data set of ship-based measurements of surface momentum  
 105 exchange – made as part of the Arctic Clouds in Summer Experiment (ACSE) in July–October 2014,  
 106 and the Arctic Ocean 2016 expedition (AO2016) in August–September 2016 – to study momentum  
 107 exchange over heterogeneous sea ice. We investigate the relationship between surface drag and sea-  
 108 ice concentration within the existing framework suggested by L2012, E2016, and its recent extension  
 109 by Lüpkes and Gryanik (2015; L2015) using over 500 new estimates of surface drag and local sea-ice  
 110 concentration measurements derived from on-board imagery, over varying sea-ice conditions and a  
 111 range of near-surface atmospheric stabilities.

112

## 113 2 Parameterization background

114 The surface flux of momentum is  $\tau = -\rho u_*^2 = \rho C_D U^2$ , where  $\rho$  is the air density,  $u_*$  is the friction  
 115 velocity, and  $U$  is the wind speed at a reference height. The drag coefficient,  $C_D$ , is derived from  
 116 Monin–Obukhov similarity theory (MOST, Monin and Obukhov, 1954) as:

$$117 \quad C_D = \kappa^2 [\ln(z/z_0) - \psi_m(\zeta)]^{-2} \quad (1)$$

118 Here,  $\kappa$  is the von Kármán constant,  $z$  is the reference height at which the transfer coefficient is  
 119 evaluated,  $z_0$  is the aerodynamic roughness length, and  $\psi_m$  is an integrated stability correction function  
 120 (Stull, 1990).

121 Over land surfaces, the aerodynamic roughness length is in general taken as constant depending upon  
 122 the surface characteristics, while over the open water the roughness length varies with wind speed and  
 123 is typically parameterized using a type of Charnock relation (Charnock, 1955). When the surface  
 124 consists of a mix of ice and open water, an effective turbulent flux over the area is usually calculated  
 125 by taking a weighted average over the fraction of open water and sea ice (Vihma, 1995):

$$126 \quad C_{D10n} = (1 - A)C_{D10nw} + AC_{D10ni}. \quad (2)$$



Here,  $C_{D10nw}$  and  $C_{D10ni}$  are, respectively, the neutral transfer coefficients for momentum over water and ice surfaces, and  $A$  is the fraction of the surface covered by ice. Over sea ice, an additional drag contribution, the form drag,  $C_{D10nf}$  is generated due to air-flow pressure against the edges of floes, leads, and melt ponds (Andreas et al., 2010; L2012; L2015; E2016). The overall equivalent neutral drag coefficient is then given by

$$C_{D10n} = (1 - A)C_{D10nw} + AC_{D10ni} + C_{D10nf}. \quad (3)$$

Lüpkes et al. (2012) proposed a hierarchical parameterization for  $C_{D10n}$  in which form drag, in its lowest level of complexity, is parameterized as a function of ice fraction only

$$C_{D10nf} = A \frac{h_f}{D_i} S_c^2 \frac{c_e}{2} \left[ \frac{\ln^2(h_f/z_{0w})}{\ln^2(10/z_{0w})} \right]. \quad (4)$$

Here,  $D_i$  is the characteristic length scale of the floe,  $h_f$  is the freeboard height,  $S_c$  is the sheltering function, and  $c_e$  is the effective resistance coefficient. Lüpkes et al. (2012) provided simplified forms for these parameters either in terms of ice fraction or as constants:

$$S_c = \left( 1 - \exp\left(-s \frac{D_w}{h_f}\right) \right), \quad (5)$$

where

$$D_w = D_i (1 - \sqrt{A}) / \sqrt{A}, \quad (6)$$

$$h_f = h_{max}A + h_{min}(1 - A), \quad (7)$$

$$D_i = D_{min} \left( \frac{A_*}{A_* - A} \right)^\beta, \quad (8)$$

and

$$A_* = \frac{1}{1 - (D_{min}/D_{max})^{1/\beta}}. \quad (9)$$

For operational purposes, L2012 suggested optimum values of the parameters used in the above expressions (Table 1). E2016 evaluated the L2012 scheme with in situ aircraft measurements and found that with slightly modified values of these key parameters (Table 1), it represented the behaviour of  $C_{D10n}$  well.

The L2012 scheme assumes that the wind profile is always adjusted to the local surface. However, this assumption is not necessarily valid where the surface conditions change over small spatial scales, and



152

	$c_e$	$S_c$	$h_f$	$\beta$	$h_{\max}$	$h_{\min}$
<b>L2012</b>	0.30	Eq. (5) with $s = 0.5$	Eq. (7)	1	0.534 m	0.286 m
<b>E2016A</b>	0.17	Eq. (5) with $s = 0.5$	Eq. (7)	1	0.534 m	0.286 m
<b>E2016B</b>	0.10	Eq. (5) with $s = 0.5$	Eq. (7)	0.2	0.534 m	0.286 m
<b>ACSE+AO2016 (P2021-L2012)</b>	0.10	Eq. (5) with $s = 0.5$	Eq. (7)	1	0.534 m	0.286 m
<b>L2015</b>	0.4	1	0.41 m	1.4	-	-
<b>L2015 (ACSE+AO2016) (P2021-L2015)</b>	0.18	1	0.41 m	1.1	-	-
<b>L2015 (ACSE data only)</b>	0.22	1	0.41 m	1.0	-	-
<b>L2015 (AO2016 data only)</b>	0.18	1	0.41 m	1.1	-	-

153

154 **Table 1:** Parameter settings for the form drag component of the L2012 scheme (Lüpkes et al., 2012, rows 1–  
 155 4): as recommended in L2012, E2016A and E2016B, P2021-L2012; and the L2015 scheme (Lüpkes and  
 156 Gryanik, 2015, rows 5–8): as recommended in L2015, and fit to ACSE+AO2016, ACSE only, AO2016 only.  
 157 The L2012 variants use:  $D_{\min} = 8$  m and  $D_{\max} = 300$  m, while the L2015 variants use  $D_{\min} = 300$  m. The primary  
 158 tuning parameter is the effective resistance coefficient,  $c_e$ , while  $\beta$  has a second order effect on the shape of the  
 159 curve.  $S_c$  and  $h_f$  were tunable parameters in L2012, but found by L2015 to have marginal impact and set as  
 160 constants for simplicity.

161

162 the fetch over the local surface is insufficient for the wind profile to come into equilibrium with its  
 163 characteristics. To overcome this issue in the existing schemes, L2015 suggested a fetch-dependent  
 164 parameterization of the form drag component of the total drag at arbitrary height:

$$165 \quad C_{Dnf} = C_{Dnf,w}(1 - A) + C_{Dnf,i}A, \quad (10)$$

166 where  $C_{Dnf,w}$  and  $C_{Dnf,i}$  are, respectively, the neutral form-drag coefficients related to the fetch over  
 167 open water and over ice, and are expressed as:

$$168 \quad C_{Dnf,k} = A \frac{h_f}{D_i} S_{c,k}^2 \frac{c_e}{2} \left[ \frac{\ln^2(h_f/ez_{0,k})}{\ln^2(z_p/z_{0,k})} \right], \text{ where } k = i, w \quad (11)$$



Thus, the L2015 scheme incorporates two form drag contributions and both are weighted by their respective surface fractions. Equation (11) differs from the formulation in L2012 (equation 4) only by the inclusion of the Eulerian number,  $e$ , in the logarithmic term of the numerator, consistent with previous work by other groups (e.g., Hanssen-Bauer and Gjessing, 1988), and is valid for any reference height,  $z_p$ . Here we evaluate L2012 and L2015 against in situ estimates of  $C_{D10n}$  to assess the impact of including form drag for both water and ice surfaces. We do not evaluate the higher levels of complexity in L2015. The values of various parameters used in the L2015 parameterization, both as originally published and tuned to our observations, are given in Table 1, along with those for L2012 and E2016.

### 3 Measurement and methods

#### 3.1 Field Measurements

We utilize data from two field campaigns, the Arctic Cloud in Summer Experiment (ACSE, Tjernström et al., 2015, 2019; Achtert et al., 2020), part of the Swedish-Russian-US Arctic Ocean Investigation on Climate-Cryosphere-Carbon (SWERUS-C3), and the Arctic-Ocean 2016 (AO2016) expedition. Both ACSE and AO2016 took place on board the Swedish icebreaker *Oden*. The ACSE cruise took place between 5 July and 5 October 2014, starting and ending in Tromsø, Norway, and working around the Siberian shelf, through the Kara, Laptev, East Siberian and Chukchi seas (Fig. 1). A change of crew and science team took place in Utqiagvik (formerly Barrow), Alaska on 20 August. The AO2016 expedition was carried out between 8 August and 19 September 2016 in the central Arctic Ocean, starting from, and returning to, Longyearbyen, Svalbard (Fig. 1).

#### 3.2 Surface turbulence and meteorological measurements

Turbulent fluxes were measured with an eddy covariance system installed at the top of *Oden*'s foremast, 20.3 m above the waterline. On ACSE this consisted of a Metek USA-100 sonic anemometer with heated sensing heads, a Li-COR Li-7500 open path gas analyser, and an Xsens MTi-700-G motion sensing package installed at the base of the anemometer. The ship's absolute heading and velocity were obtained from its navigation system. The Metek sonic anemometer failed at the start of AO2016 and was replaced with a Gill R3 sonic anemometer. The raw turbulent wind components, at 20 Hz, were corrected for platform motion following Edson et al. (1998) and Prytherch et al. (2015). Corrections for flow distortion of the mean wind were derived from a CFD model (Moat et al. 2015). Turbulent fluxes of heat, momentum and moisture were estimated by the eddy-covariance technique over 30-min averaging intervals.



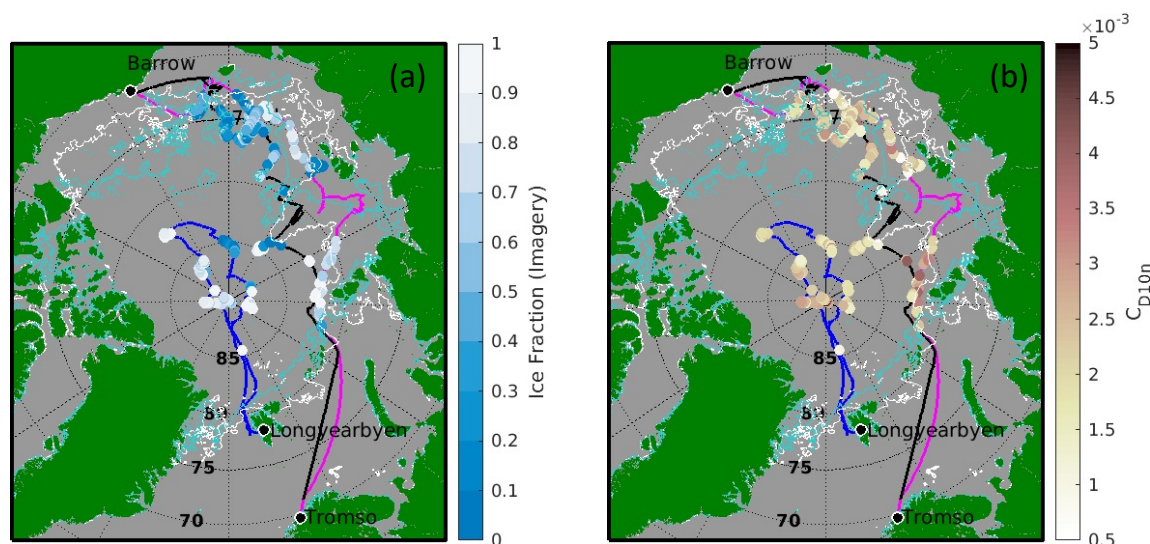


**Figure 1.** The cruise tracks of ACSE (leg 1, 5 July – 18 August 2014 (magenta) and leg 2, 21 August – 5 October (black) and AO2016 (8 August – 19 September 2016, (blue)) with (a) sea-ice fraction from in situ imagery and (b)  $C_{D10n}$ , for each 30-min flux period shown. The sea-ice extent from AMSR2 on 7 August 2014 (white) and 2016 (cyan) – about midway through ACSE and at the start of AO2016 – are shown for reference and to give an indication of the variability between years.

Mean temperature ( $T$ ) and relative humidity ( $RH$ ) at the mast top were measured with an aspirated sensor – a Rotronic T/RH sensor during ACSE and a Vaisala HMP-110 during AO2016. Additional  $T$ ,  $RH$  and pressure ( $P$ ) measurements were made by a Vaisala PTU300 sensor on the 7th deck of the ship. Pressure at the mast top was obtained by height-adjusting the measurement from the 7th deck. The surface skin temperature was obtained from two Heitronics KT15 infra-red surface temperature sensors, mounted above the bridge and viewing the surface on either side of the ship. Digital imagery of the surface around the ship was obtained from 2 Mobotix M24 IP-cameras mounted on the port and starboard beam rails above the bridge, approximately 25 m above the surface. Images were recorded at 1-minute intervals during ACSE and 15-second intervals during AO2016. Profiles of atmospheric thermodynamic structure and winds were obtained from Vaisala RS92 radiosondes, launched every 6 hours throughout both cruises. During ACSE a Radiometer Physics HATPRO scanning microwave radiometer provided additional retrievals of lower-atmosphere temperature profiles every 5 minutes.

### 3.3 Estimation of turbulence parameters and data screening

The transfer coefficient of momentum is computed as:



$$C_{D10n} = \left( \frac{u_*}{U_{10n}} \right)^2 \quad (12)$$

where  $u_*$  is the measured friction velocity, and  $U_{10n}$  is the 10 m equivalent neutral wind speed, determined using Monin-Obukhov similarity theory and Businger-Dyer stability corrections (Businger et al., 1971).

A total of 3421 and 1555 individual half hourly flux estimates were obtained during ACSE and AO2016 respectively. Data were removed from the analysis if they failed a set of flux quality control criteria (Foken and Wichura, 1996) resulting in a subset of 1804 (247) flux estimates. Additional quality control criteria were applied to filter out data unreliable for analysis of transfer coefficients:

- The relative wind direction was restricted to  $\pm 120^\circ$  from bow-on, where the flow is clear of the ship's superstructure.
- Data points where the stability parameter,  $z/L$  (where  $L$  is the Obukhov length) was greater than 1 or less than  $-2$  were removed to avoid the effects of strong stability and instability.
- Sign constancy between the turbulent heat flux and mean gradients was enforced. The Richardson number,  $Ri_b$ , and  $z/L$  should always have same sign, while the sensible heat flux,  $H$ , should be of opposite sign to  $z/L$ . Inconsistencies may arise due to combined measurement uncertainties where the temperature gradient or  $H$  are small.
- Data were also removed where the 10-m wind speed was less than  $3 \text{ m s}^{-1}$ .

After initial quality control we have a total of 1403 and 162 half hourly flux estimates. For ACSE data an additional quality control criterion was applied based on the boundary-layer profiles. Working around the MIZ, ACSE experienced multiple warm air advection events. These result in strong near-surface air mass modification and the formation of very low or surface-based temperature inversions (Tjernström et al., 2019) which can exhibit significant spatial and temporal variability. Temperature profiles from the HATPRO microwave radiometer, bias-corrected through extensive comparisons with 6-hourly radiosondes, were used to detect surface inversions with 5-minute temporal resolution following Tjernström et al. (2019). The profiles were classified as surface-based inversions, low-level inversions (inversion base height  $< 200 \text{ m}$ ), and well-mixed boundary layers (inversion base height  $> 200 \text{ m}$ ). The flux periods with mixed surface-based and low-level inversions were discarded from the analysis on the basis that the change in near-surface thermodynamic structure was likely to compromise the quality of the flux-profile relationship upon which the calculation of  $C_{D10n}$  depends. Following this step, we were left with 1051 data points from the ACSE campaign. No high-frequency profile measurements were available from AO2016; however, operating much further from the ice



edge, AO2016 was not subject to the frequent warm air advection and air mass modification events seen during ACSE.

255

### 3.4 Determination of sea-ice concentration

Estimates of sea-ice fraction are drawn from two sources: (i) a local estimate of ice fraction determined from digital imagery from the ship; and (ii) daily ice fractions, derived from satellite based Advanced Microwave Scanning Radiometer (AMSR2) passive microwave measurements (Sprenn et al., 2008).

Our local raw imagery consists of high-definition (2048×1536) images of the surface to port and starboard, obtained from Mobotix MX-M24M IP cameras mounted above the ship's bridge, 25 m above the surface. Additional images from a camera pointed over the bow are used for visual inspection while selecting the periods when *Oden* was in the ice, but not processed because the ship dominates the near field of the image.

On-board imagery can provide local surface properties including sea ice and melt pond fractions with a spatial resolution of order metres on a time base matched to the flux averaging time (Weissling et al., 2009). The large volume of imagery sampled requires automated image processing techniques to estimate ice properties (Miao et al., 2015; Perovich et al., 2002; Renner et al., 2014; Webster et al., 2015; Wright and Polashenski, 2018). Here we use the Open Source Sea-ice Processing (OSSP) algorithm of Wright and Polashenski (2018). The surface properties obtained during each 30-minute interval are averaged to give the sea ice and melt pond fractions. The image processing methodology is described in Appendix A. Limitations on quality and availability of imagery resulted in a further 206 (36) flux estimates for the ACSE (AO2016) datasets being discarded. After all quality control criterion are applied and flux estimates matched with robust estimates of the local ice fraction, we retain at total of 542 flux estimates: 416 from ACSE and 126 from AO2016. Initially melt ponds are treated as open water; the impact of this is examined in Appendix B.

Satellite-based sea ice products are widely used to prescribe ice concentration in operational forecast models and have been used to assess the dependence of in situ flux measurements as a function of ice fraction (e.g., Prytherch et al., 2017). However, they have significant uncertainties when related to in situ flux measurements due to their relatively coarse temporal and spatial resolution (Weissling et al., 2009) resulting in a mismatch between the satellite footprint and that of the surface flux measurement, and the times of the measurements. The AMSR2 satellite measurements used here provide *daily* sea-ice concentration on a 6.25 km grid, while eddy covariance flux estimates are for 30-minute periods



284 and have a footprint of the order of a few hundred metres to a kilometre. The AMSR2 estimates are  
285 interpolated spatially to the locations of each flux measurement.

286

## 287 **4 Results**

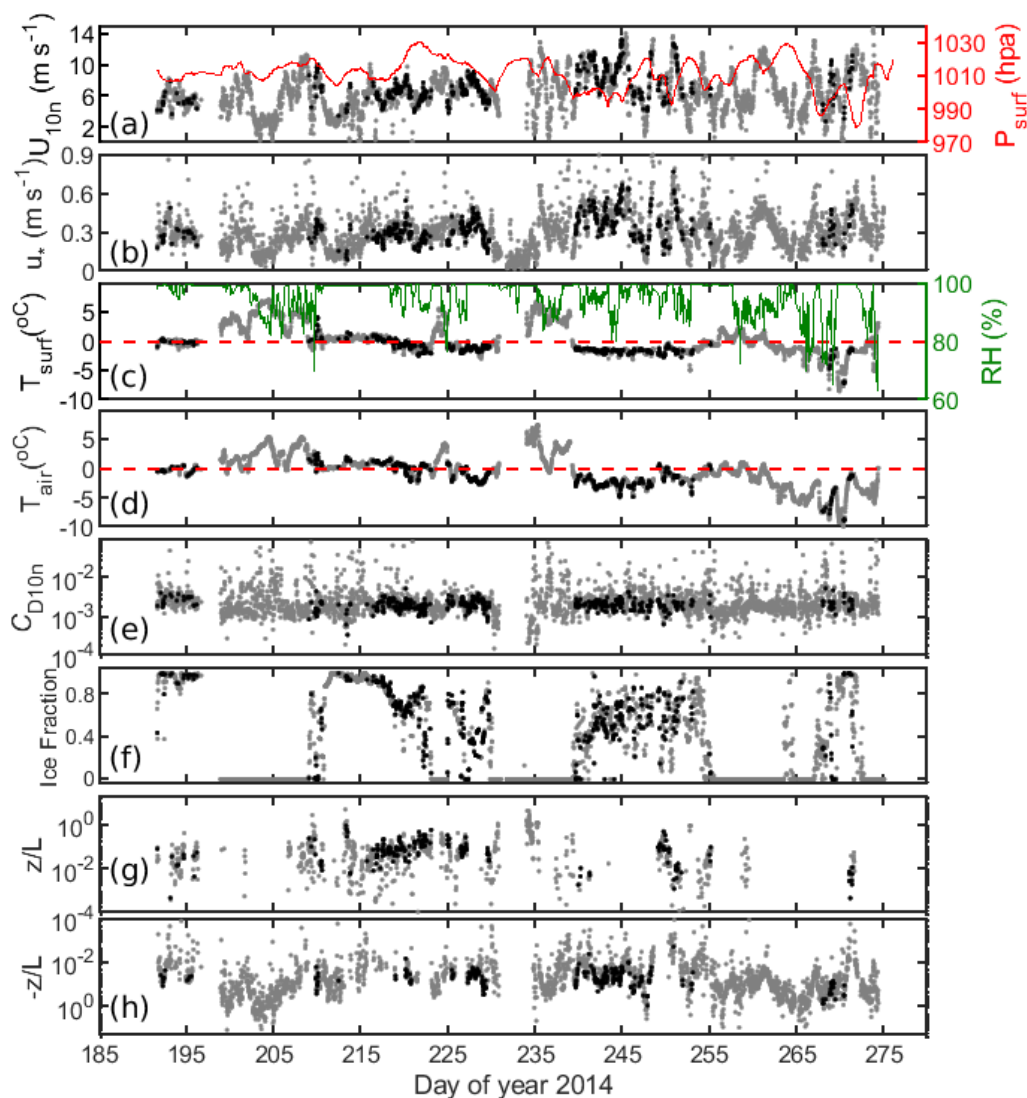
### 288 **4.1 Atmospheric conditions during ACSE and AO2016**

289 Figures 2 and 3 show the meteorological and surface conditions during ACSE and AO2016. The first  
290 half of ACSE was dominated by relatively low winds, and surface temperatures close to 0°C when in  
291 the ice; much warmer temperatures are associated with open coastal waters. The second half of the  
292 cruise experienced higher, and more variable winds, associated with multiple low-pressure systems.  
293 Temperatures first fell to the freezing point of salt water on day of year (DoY) 218, although  
294 Sotiropoulou et al. (2016) identified the start of freeze up as DoY 241. AO2016 saw a shift from  
295 relatively low surface air pressure, and mostly low winds to higher pressure and more variable winds  
296 with frequent occurrence of high winds around DoY 237.

297 Out of the total of 542 flux estimates, we have 184, 282, and 76 flux estimates in stable ( $z/L > 0.01$ ),  
298 near-neutral ( $-0.01 < z/L < 0.01$ ), and unstable conditions ( $z/L < -0.01$ ) respectively. This distribution  
299 in static stability augments the limited data sets already available over the marginal ice zone, which  
300 have been predominantly in unstable conditions (e.g., E2016).

### 301 **4.2 Ice surface characteristics**

302 Figure 4 shows the variation over time of the ice, melt pond, and open water fractions determined from  
303 the on-board imagery and from AMSR2. Note that the variations represent geographic variability along  
304 the cruise tracks, as well as temporal changes in ice conditions. During the early phase of the ACSE  
305 campaign, to mid-July (DoY 185 to 196), the ice encountered was mostly old ice (Tjernström et al.,  
306 2019) with an average ice concentration of about 70%; melt ponds and open water had 11% and 18%  
307 coverage respectively. In this phase the average concentration from AMSR2 was 95% – larger than  
308 the sum of average local ice and melt pond concentrations (81%). From late July to early August (DoY  
309 209 to 229), the average local ice concentration was 56%, with melt pond and open water fractions of  
310 about 17% and 27%. Here the AMSR2 concentration was lower than that from imagery, at 44%.  
311 During this period, warm continental air from Siberia flowed northward across the *Oden's* track  
312 causing a rapid melting of ice (Tjernström et al., 2015; Tjernström et al., 2019). From late August to  
313 mid-September (DoY 239 to 255), the average local concentration declined to 27.6% and the surface



314

315

316 **Figure 2.** Time series of (a) 10 m neutral wind speed,  $U_{10n}$  and Surface pressure,  $P_{surf}$ , (Secondary axis), (b)  
 317 friction velocity,  $u_*$  (c) surface temperature,  $T_{surf}$  and relative humidity, RH, (Secondary axis), (d) air  
 318 temperature,  $T_{air}$ , (e) 10 m equivalent neutral drag coefficient,  $C_{D10n}$  (f) Ice fraction from AMSR2 satellite, (g)  
 319 Monin-Obukhov stability parameter,  $z/L$ , for  $z/L > 0$  (stable) and (h)  $z/L < 0$  (unstable), for ACSE data. The  
 320 grey dots are 30-minute flux periods from the whole cruise, while the black dots correspond to the flux data  
 321 points that pass quality control. In panels (c) and (d), the dashed red lines show  $T_{air} = T_{surf} = 0^\circ\text{C}$ .

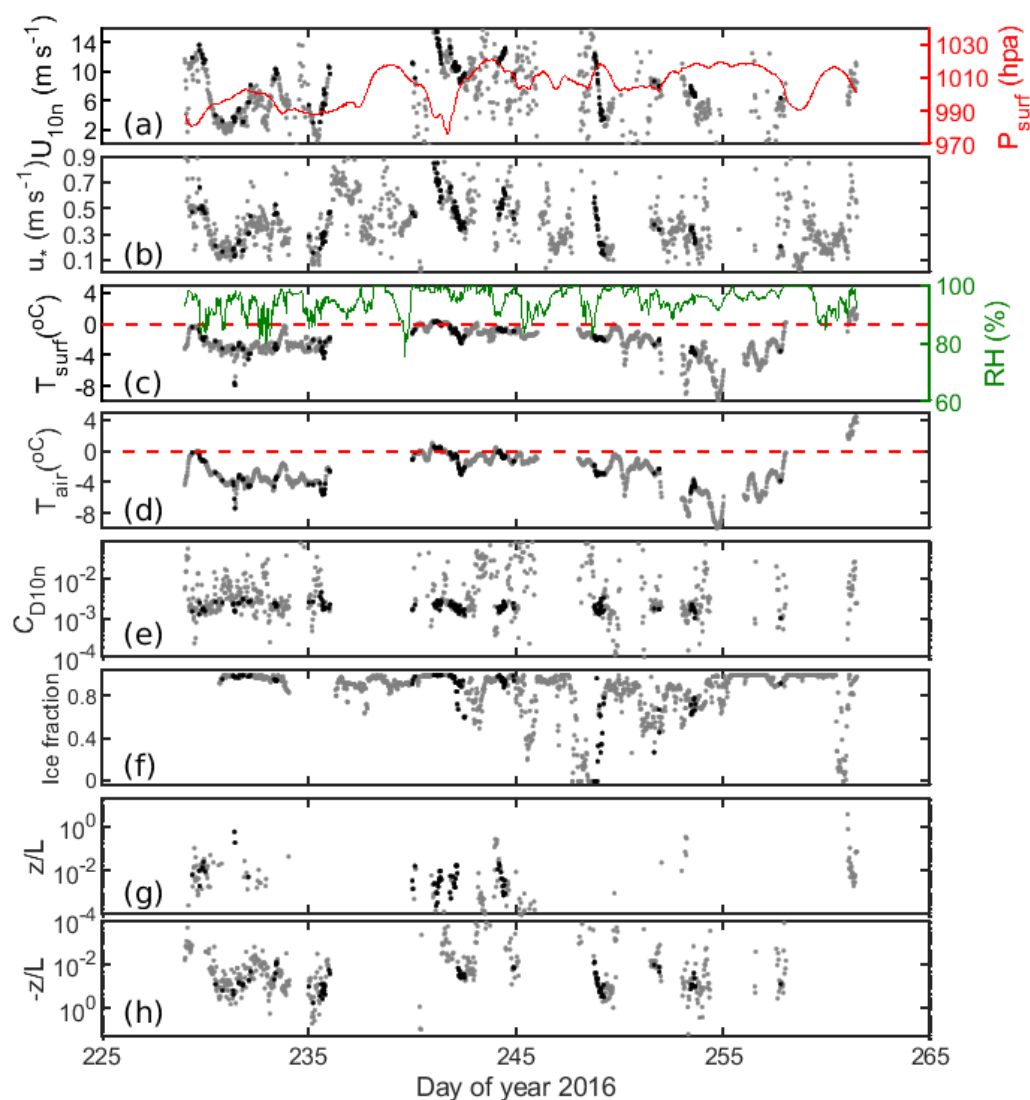


**Figure 3.** As Figure 2 but for AO2016.

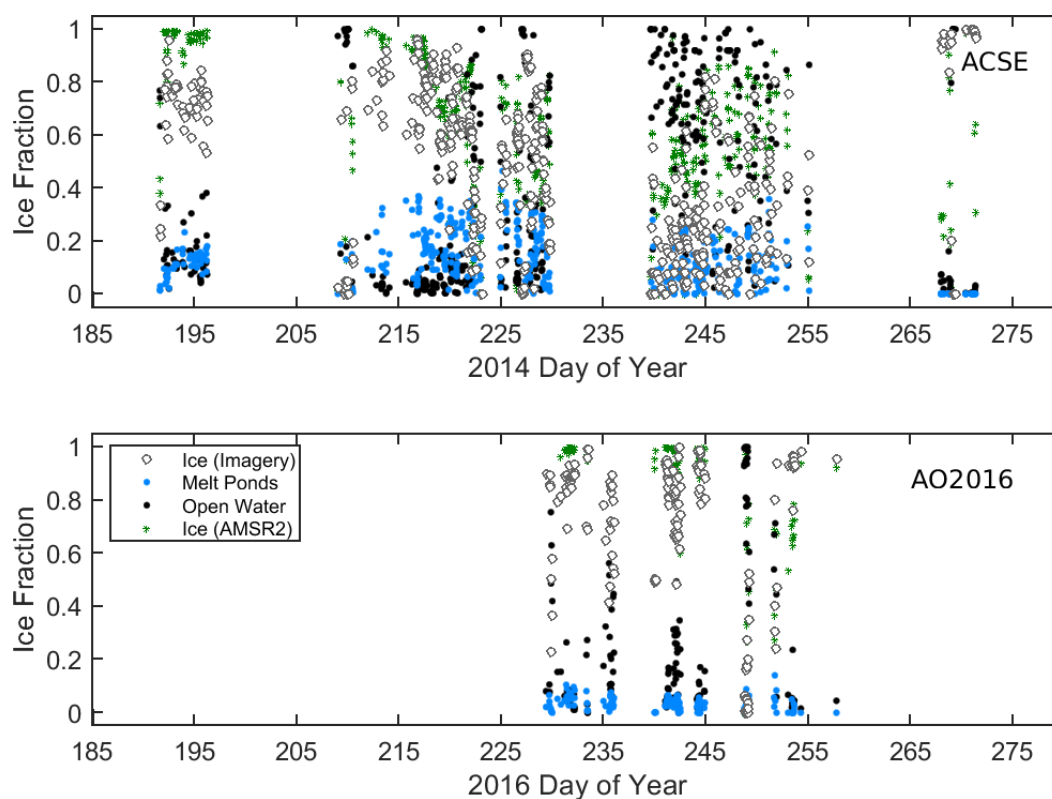
was mostly characterized by large areas of open water (63%). The AMSR2 ice fraction was 54%, approximately twice that from the imagery. During late September (DoY 268 to 272), a large variation in the surface conditions was observed and often the ice concentration was higher than 90% due to the presence of newly formed thin ice, nilas, and pancake ice. During the AO2016 campaign, the surface was mostly characterized by old and thick ice with intermittent patches of thin ice and melt ponds,





330 reflecting the more northerly cruise location. The average ice concentrations from imagery and  
 331 AMSR2 were found to be about 80% and 90% respectively.

332



333

334 **Figure 4.** Time series of ice, melt pond and open water fractions (white, blue and black symbol respectively)  
 335 from the local imagery, and ice fraction (green) from AMSR2, interpolated to the ship location. The top panel  
 336 is for ACSE and the bottom panel for AO2016.

337

338 Figure 5 shows a direct comparison of ice fraction from the in situ imagery and AMSR2. There is a  
 339 broad correspondence, but a very high degree of scatter, and AMSR2 tends to overestimate the local  
 340 sea-ice fraction; the correlation coefficient, mean absolute bias, and root mean square error are 0.64,  
 341 0.21, and 0.28 respectively. It is clear from the ice concentration time series, however, that the bias  
 342 between AMSR2 and local ice fraction varies over time and appears to be related to the surface  
 343 conditions of melt or freeze up, in particular when changes are rapid. The largest difference between  
 344 ice fraction from both projects was found during the early freeze-up season where there is extensive  
 345 very thin ice.

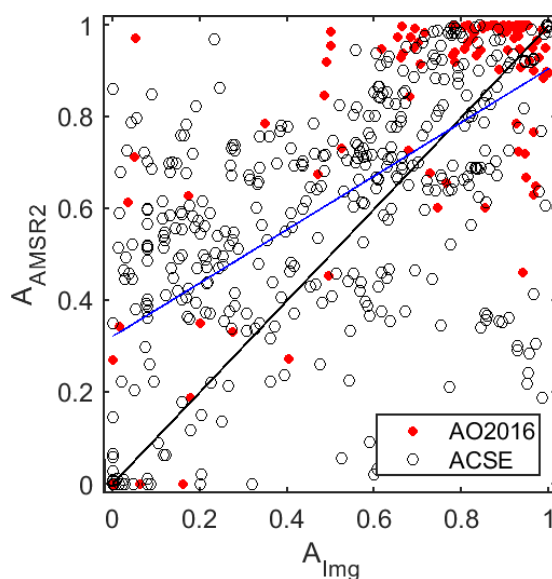


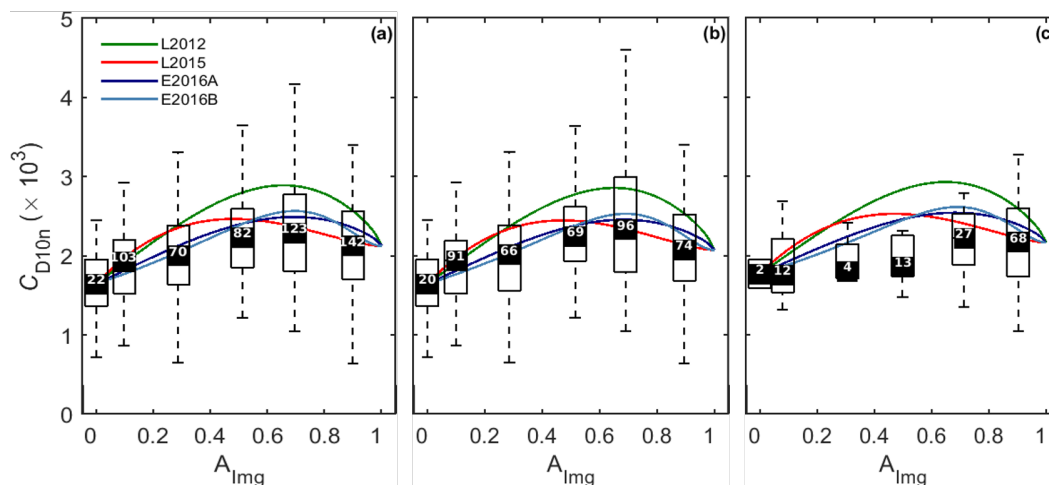
**Figure 5.** A comparison of ice fraction derived from the local imagery and from AMSR2 for both field campaigns. The linear regression ( $A_{\text{AMSR}} = 0.584A_{\text{img}} + 0.321$ ) and 1:1 lines are shown in blue and black respectively.

### 4.3 Variation of momentum transfer coefficient with sea-ice concentration

We first assess the variability of surface drag with sea-ice fraction using local ice concentration from the on-board imagery (Fig. 6). The range and median values of  $C_{\text{D10n}}$  over sea ice ( $A_{\text{img}} > 0$ ) are similar to those of previous studies (Banke and Smith, 1971; Overland et al, 1985; Guest and Davidson, 1987; Castellani et al., 2014; Elvidge et al., 2016). The peak  $C_{\text{D10n}}$  is found at 0.6–0.8 ice fraction bin, consistent with Lüpkes et al. (2012) and Elvidge et al. (2016). The median values of  $C_{\text{D10n}}$  in both datasets agree well for high ice fractions (Figs. 6b and 6c), however, there is insufficient AO2016 data for  $A_{\text{img}} < 0.5$  to make a robust comparison with ACSE. Given the good general agreement between ACSE and AO2016 we will only consider the joint data set from here on.

The measurements are compared with the L2012, L2015, and E2016 parameterization schemes. Note that these all require specified values of  $C_{\text{D10n}}$  over open water ( $A_{\text{img}} = 0$ ) and solid ice ( $A_{\text{img}} = 1$ ) (see Eq. 2); these vary with conditions, dramatically so for  $A_{\text{img}} = 1$ , as demonstrated by Elvidge et al. (2016). Here, we follow E2016 and fix the values of  $C_{\text{D10nw}}$  and  $C_{\text{D10ni}}$  used in the parameterizations to the measurements, using the observed median values at  $A_{\text{img}} = 0$  and  $A_{\text{img}} > 0.8$  respectively for each





366

367 **Figure 6.**  $C_{D10n}$  as a function of ice fraction as derived from local imagery ( $A_{img}$ ) for (a) the joint ACSE and  
 368 AO2016 datasets ( $n = 542$ ), (b) the ACSE dataset ( $n = 416$ ), (c) the AO2016 dataset ( $n = 126$ ). The boxes show  
 369 the interquartile range and the bin median (black square) for bins of width = 0.2 and plotted at the mean ice  
 370 fraction for the bin; the number of data points in each bin is noted at the median level. Whiskers indicate the  
 371 range of the estimates, excluding any outliers, which are plotted individually if present. Parameterization  
 372 schemes are overlain as indicated, with each curve anchored at the observed median values of  $C_{D10nw}$  ( $A_{img} = 0$ )  
 373 and  $C_{D10ni}$  (defined here as  $A_{img} > 0.8$ ) for each data set.

374

375 data set. Note that  $A > 0.8$  is used, as opposed to  $A = 1$ , as navigational consideration meant the ship  
 376 rarely operated in regions with an ice fraction of 1. The mean ice fraction in this bin is 0.89. Here, we  
 377 do not adjust any of the other tuneable parameters in these parameterizations.

378 L2012 overestimates the observations of all but the lowest ice concentrations. E2016a and E2016b –  
 379 which follow L2012 with settings tuned to measurements over the MIZ from Fram Strait and the  
 380 Barents Sea – correspond well with the observations, with only a slight overestimate of the peak values.  
 381 L2015, which accounts for form drag over water as well as over ice, is a close match to the observations  
 382 for  $A_{img} > 0.6$  but overestimates the 0.2–0.4 and 0.4–0.6 bins and peaks at too low an ice concentration.  
 383 Note we will tune the L2015 scheme using our measurements in section 4.4.

384 The median value of  $C_{D10n}$  at  $A = 0$  was  $1.65 \times 10^{-3}$ , which is higher than those typically found over the  
 385 open ocean (Smith, 1980; Large and Yeager, 2009; Andreas et al., 2012). This may be a result of the  
 386 open water measurements being made under fetch-limited conditions close to the ice edge, or within  
 387 regions of open water within the pack ice, where an under-developed wave state may result in higher  
 388 drag (Drennan et al., 2003). We cannot, however, exclude the possibility that they result from an



incomplete correction for flow distortion over the ship (Yelland et al. 1998, 2002), or that the flux footprint includes flow over nearby ice that is not visible in the imagery.

Figure 7 shows  $C_{D10n}$  as a function of AMSR2 ice fraction. There is broad agreement with the values in Fig 6a at low and high ice concentrations, but there is no peak in  $C_{D10n}$  at intermediate concentrations. Instead, the measurements with higher drags have moved to either lower or higher ice fraction bins. This is not consistent with either our in situ imagery or previous aircraft-based studies, suggesting it is a limitation of the AMSR2 imagery.

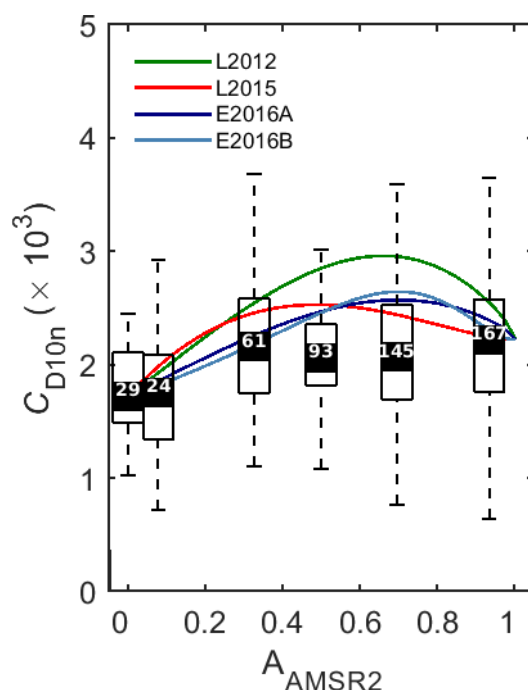


**Figure 7.** As Figure 6a but for ice fraction derived from AMSR2 satellite.

#### 4.4 Updating parameterizations using local sea-ice concentration measurements

L2015 extended the parameterization of L2012 to explicitly represent the impact of fetch dependence over heterogeneous surfaces in a physically consistent manner. To date this scheme is unconstrained by observational data. Here, we validate the scheme and provide recommendations for its tuneable parameters based on the joint ACSE and AO2016 data sets. E2016 pointed out that variation in the

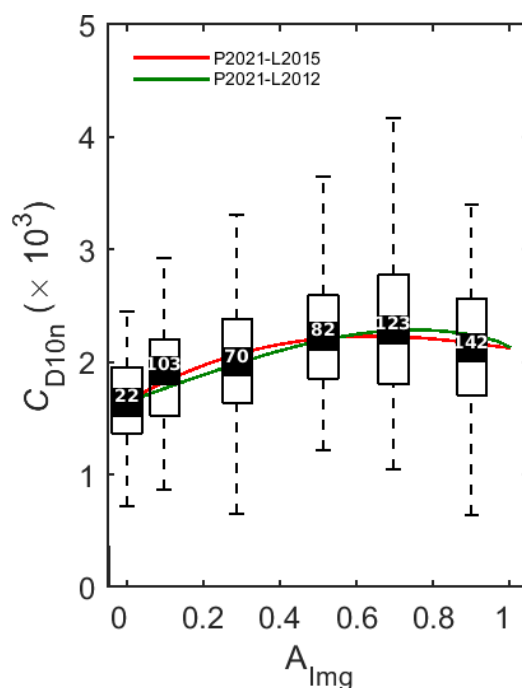


405 morphological parameters  $\beta$  and  $c_e$  in L2012 could explain the variability of  $C_{D10n}$  within concentration  
 406 bins. Reducing the values of  $\beta$  and  $c_e$  from those suggested by L2012 resulted in a better fit to their  
 407 data.

408 In the fetch dependent L2015 parameterization, increasing  $\beta$  (sea-ice morphology exponent, Eq. 8 and  
 409 9) results in decreasing  $C_{D10n}$ , mostly at high ice concentrations, while increasing  $c_e$  (the effective  
 410 resistance coefficient) increases  $C_{D10n}$  at all concentrations. Here we have adjusted the L2015 values  
 411 of  $\beta$  and  $c_e$  to optimise the fit to our measurements. The revised values of the coefficients are given in  
 412 Table 1. For a consistent comparison, a similar tuning is applied to L2012.

413 Figure 8 shows  $C_{D10n}$  plotted against  $A_{img}$  along with the tuned L2015 and L2012 schemes, both  
 414 anchored to the observed values of  $C_{D10n}$  at  $A_{img} = 0$  and  $A_{img} > 0.8$  for the joint dataset.

415



416

417 **Figure. 8**  $C_{D10n}$  as function of local ice fraction ( $A_{img}$ ) for the joint ACSE and AO2016 ( $n = 542$ ) dataset. Here,  
 418 the proposed parameterization (red line, P2021-L2015) is presented with L2015 anchored at the observed values  
 419 of  $C_{D10nw}$  ( $A_{img} = 0$ ) and  $C_{D10ni}$  ( $A_{img} > 0.8$ ) with coefficients  $\beta$  and  $c_e$  shown in Table 1. For comparison, the  
 420 L2012 schemes (green line, P2021-L2012) is also tuned with curve anchored at the same values of  $C_{D10ni}$  and  
 421  $C_{D10nw}$  with  $\beta$  and  $c_e$  shown in Table 1.



Both L2012 and L2015 provide an excellent fit to the data, passing close the median observed values at all ice fractions. The fitted curve for the joint dataset works equally well for the individual datasets (Fig. S1, Supplementary material).

In the analysis above we have considered  $C_{D10n}$  as a function of ice fraction – no distinction is made between melt ponds and open water. However, there are uncertainties in the surface classification, in particular for the determination of melt pond fraction. Thin ice and shallow melt ponds can appear very similar in colour, and potentially be misclassified by the image processing algorithm. An assessment of the sensitivity of the fitting of the L2015 to the presence and treatment of melt ponds (see appendix B) shows that they have little impact.

Melt ponds are explicitly included in the L2012 and L2015 parameterizations in their more complex levels of implementation, where the edges of melt ponds provide a source of form drag. Tsamados et al. (2014) modelled the different contributions to the total drag using L2012 implemented within the CICE sea ice model (Hunke and Lipscomb, 2010). They found that melt ponds made a negligible contribution to the drag except over the oldest, thickest ice just north of the Canadian archipelago, consistent with our observations.

Both L2012 and L2015 can be tuned to provide excellent fits to the observations (Fig 8). Even without tuning to this data set, the differences between L2015, E2016A and E2016B are modest and all lie within the interquartile range of the observed  $C_{D10n}$  at all ice fractions (Fig 6a). The largest source of uncertainty in the application of these schemes is the value of the drag coefficient at 100% ice fraction,  $C_{D10ni}$ , which must be prescribed, and is strongly dependent on ice morphology. Table 2 lists values of the neutral drag coefficient for very high ice fractions (0.8–1 from this study, and 0.9–1 or 1 in previous studies) reported in the literature. The best estimates (mean or median values) vary by a factor of more than 4. As discussed in previous studies,  $C_{D10ni}$  depends on the sea-ice morphology and so prescribing this as one value is a drastic simplification.



$C_{D10nl} (x10^{-3})$			N	Location/Morphology	Reference
Median or mean	Interquartile range or $\pm s$	Full range			
2.1	1.3–2.8	0.4–5.5	74	Eastern Arctic (ACSE)	This study
2.2	1.6–2.7	1.1–3.3	68	Central Arctic (AO2016)	This study
3.4	2.5–4.2	1.8–5.7	24	Iceland Sea	Elvidge et al. (2021)
2.6	2.4–3.9	1.9–4.0	8	Barents Sea (broken floes)	Elvidge et al. (2016)
0.9	0.4–2.1	0.1–3.8	32	Fram Strait (large flat floes)	Elvidge et al. (2016)
1.9	1.5–2.2			Fram Strait (REFLEX I & II)	Lüpkes & Birnbaum (2005)
1.5				Fram Strait (REFLEX)	Mai et al. (1995)
3.8	2.5–5.1			Very rough floes	Guest & Davidson (1987)
1.5	1.2–1.9	1.2–1.9		Large flat floes	Table 2, Overland (1985)
	1.7–2.6	1.7–3.7		Rough ice with ridges	Tables 3,6, Overland
	2.2–2.7			Marginal Seas, broken ice	Table 6, Overland

**Table 2** Overview of neutral drag coefficients based on in situ eddy covariance measurements over ‘complete’ sea-ice cover ( $C_{D10nl}$ ) from this and previous studies. The values are taken from the literature, so vary as to whether the mean, median or a range of values is shown. The definition of ‘complete’ sea ice covers a range of ice fractions (0.8–1, 0.9–1.0, and exactly 1) depending on the study. N is the number of data points in this bin where specified. The 2<sup>nd</sup> column provides the interquartile range or the range from  $-1s$  to  $+1s$ , where  $s$  is the standard deviation. Note Guest and Davidson (1987) uses the turbulence dissipation method. Overland (1985) compiles values from a variety of previous studies in various locations, as well as new data, so the values reproduced here are a compilation by morphology.

## 5 Conclusions

An extensive set of measurements of drag coefficients over sea ice, obtained during two research cruises within the Arctic Ocean, has been utilized to evaluate the dependence of drag on ice fraction. The final data set consists of 542 estimates of drag coefficients along with estimates of the local ice fraction obtained from high resolution imagery of the surface around the ship. The measurements cover a wide geographic area, summer melt and early autumn freeze up, and a range of surface conditions from thick multiyear ice, through melting ice with melt ponds, to newly formed thin and pancake ice, and near-surface stability conditions of  $-2 < z/L < 1$ , a much wider range than E2016. This wide range of conditions means the results should be broadly representative of much of the Arctic sea ice region.

The dependence of  $C_{D10n}$  on ice fraction is evaluated in the context of recent, state-of-the-art parameterization schemes (Lüpkes et al., 2012; Lüpkes and Gryanik, 2015). The most recent of these (Lüpkes and Gryanik, 2015) attempts to account for the impact of short fetch over ice/water over



473 spatially highly heterogeneous surfaces. When tuned to the observations, the parameterizations provide  
474 an excellent representation of  $C_{D10n}$  as a function of ice fraction:

475 The main conclusions are:

- 476 • The data support the existence of a negatively skewed distribution of  $C_{D10n}$  with ice  
477 concentration, with a peak value for fractions of 0.6–0.8, consistent with the predicted  
478 behaviour from Lüpkes et al. (2012) and observations of Elvidge et al. (2016).
- 479 • When tuned to our measurements, both L2012 and L2015 provide an excellent fit to the  
480 observed variation of  $C_{D10n}$  with ice fraction. The impact of small-scale surface heterogeneity  
481 and the influence of fetch is likely to increase with increasing contrast in the skin temperatures  
482 of the ice and water surfaces, and thus play a greater role in the winter.
- 483 • Melt ponds had no significant impact on the drag coefficient over the study area. The optimum  
484 fit of the L2015 parameterization to the measurements had little sensitivity to the uncertainty  
485 in partitioning of melt ponds to the ice or water fractions when estimating the local ice fraction;  
486 and there was little sensitivity to the presence of melt ponds at all for the conditions observed.
- 487 • When evaluated against the AMSR2 retrieval of ice fraction, the behaviour of  $C_{D10n}$  is not  
488 consistent with in situ observations, for example, no peak is seen at intermediate ice fractions.  
489 This is likely a result of several factors: a mismatch in spatial scale between the in situ flux  
490 footprint (of order 100s of metres to 1 km) and the satellite footprint (6.5 km); potential spatial  
491 offsets in location matching resulting from the low temporal resolution of the satellite data  
492 (daily retrievals) combined with drifting of the ice; and the high scatter and varying mean bias  
493 between the in situ and satellite estimates of ice fraction. The mean bias in particular displays  
494 temporal/spatial coherence that suggests a dependence upon surface conditions. This finding  
495 cautions against the use of comparatively low resolution remote-sensing products when  
496 evaluating parameterizations.

497 Atmospheric stability may also play a role here, since it will affect how rapidly the atmospheric surface  
498 layer adjusts to changes in surface properties. L2015 incorporates stability effects in the higher levels  
499 of parameterization complexity, but not within the simplest complexity level used here. A much larger  
500 data set, including the details of surface heterogeneity, would be required to evaluate the details of  
501 both stability and fetch dependencies.

502 Sea ice and climate models are starting to incorporate components of form drag within their surface  
503 exchange schemes for sea ice (e.g., Tsamados et al., 2014; Renfrew et al., 2019). But at present, most



504 do not use all the components of the more complex versions of schemes such as L2012 or L2015.  
505 Instead, they tend to rely on the simplest versions where drag is only a function of ice fraction. In  
506 operational forecast models, where only a prescribed ice concentration from a satellite retrieval may  
507 be available, this seems appropriate, but within more complex coupled weather and climate prediction  
508 models there is the potential for using output from the sea-ice model to adjust the drag coefficient  
509 (E2016; Renfrew et al., 2019). The skill of the parameterization is strongly dependent on the accurate  
510 representation of the drag at 100% ice fraction,  $C_{D10ni}$ , which varies significantly with ice morphology  
511 (Lüpkes et al., 2012; Lüpkes and Gryanik, 2015; Elvidge et al., 2016, 2021). Tackling the  
512 representation of  $C_{D10ni}$  should be the next challenge in improving air-ice surface drag in weather and  
513 climate models.

514



## 515 **Appendix A: Image processing and evaluation of local ice fraction**

516

517 A total of ~500,000 images of the surface around the ship were obtained over the two cruises, so this  
518 required an automated approach to estimate the local ice fraction. Here we use the Open Source Sea-  
519 ice Processing (OSSP) algorithm of Wright and Polashenski (2018).

### 520 **(a) Pre-processing:**

521 Of the images available for each flux period, a subset of visibly good images was selected for further  
522 processing. The rejection of images was due to the presence of dense fog, moisture or ice on the camera  
523 lens, strong surface reflection of direct sunlight, or insufficient illumination. The selected subsets  
524 consist of 10 to 60 images in each flux period (e.g., Fig. A1(a)). These images are first corrected for  
525 lens distortion. The lens specific distortion coefficients and intrinsic parameters were determined using  
526 the Computer Vision System Toolbox of MATLAB. The corrected images (2048×1536 pixels) were  
527 then cropped to select a region within ~200m of the ship (2009×1111 pixels) – e.g., see Fig. A1(b).

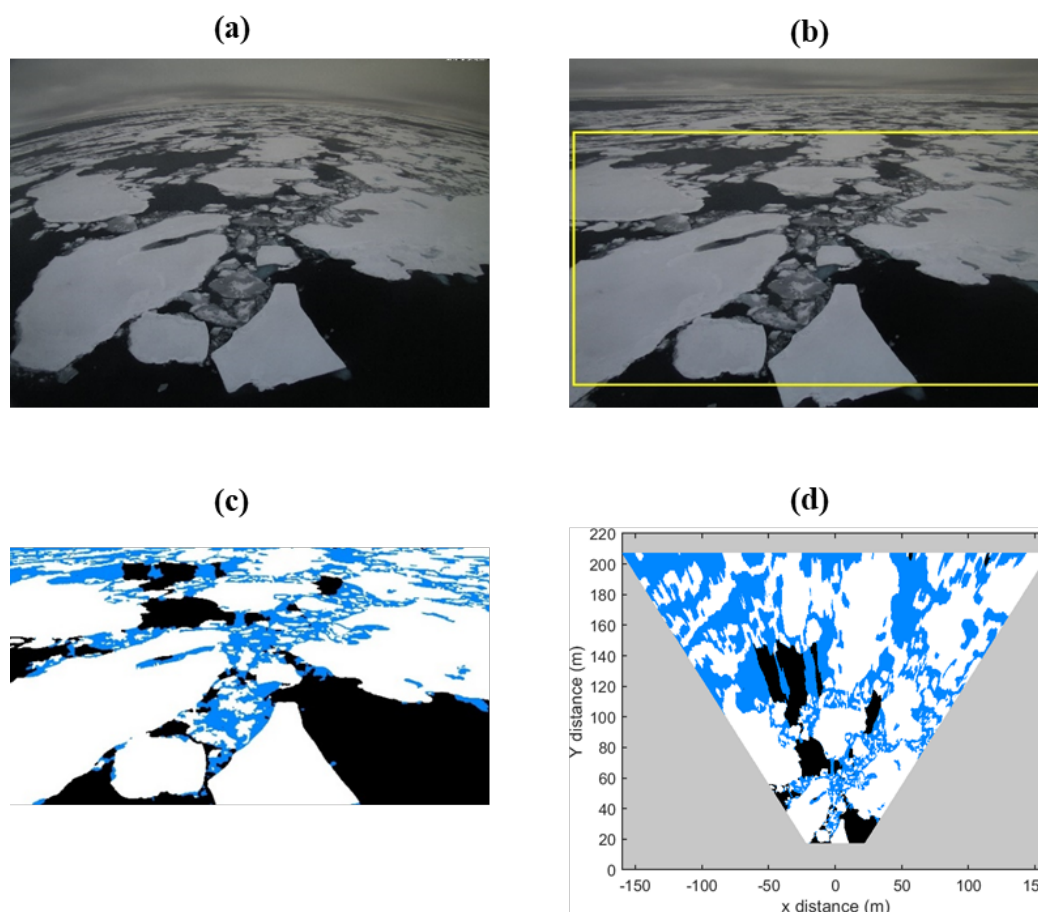
### 528 **(b) Training and implementation of the algorithm:**

529 The success of any machine learning-based algorithm depends upon the quality of the training dataset.  
530 Since the ice conditions varied substantially throughout the campaigns, extensive training data was  
531 needed to cover the wide range of conditions. The initial training images selected were from the first  
532 and last image from each flux period. Additional images were added iteratively depending upon the  
533 performance of the algorithm on randomly selected images. After multiple trials, we settled on three  
534 different training datasets for (i) images with visibly large ice fraction, (ii) images with large open  
535 water fraction, (iii) images showing newly formed thin ice. Our approach was to generate a training  
536 data set that could be utilized equally on imagery from other campaigns, while keeping the number of  
537 discrete training datasets as small as possible. The training data, identifying ice, water, and melt-ponds  
538 was generated based on user classification of the training images via a Graphical User Interface (GUI),  
539 and thus depends upon the ability of the user to identify the surface features correctly.

### 540 **(c) Post-processing:**

541 The OSSP algorithm produces an indexed image having pixel-wise information about surface features  
542 (open water, melt ponds, ice) for each input image (e.g., Fig. A1(c)). Since the images were necessarily  
543 taken at an oblique angle, the indexed images need to be orthorectified to derive the correct fractions  
544 of ice, melt pond and water. Orthorectification of imagery is a process by which pixel elements of an  
545 oblique image are restored to their true vertical perspective position. The angular separation of each





546

547

548 **Figure A1.** An example of the image processing workflow. Panel (a) is an example raw image; (b) shows the  
 549 image corrected for the lens distortion, where the region of focus is shown by the yellow rectangle; (c) shows  
 550 the image after processing by the OSSP algorithm where the masking colours – white, blue and black – represent  
 551 ice, melt pond/submerged ice and open water areas, respectively; (d) shows the orthorectified image showing  
 552 the true distance of each surface feature away from the camera.

553

554 pixel (after correction for lens distortion) was determined from a lab calibration of the cameras. The  
 555 angle from the horizon (the horizontal) in the images, and the height of the camera above the surface  
 556 then allows the location of each pixel on the surface to be calculated. The masked images were  
 557 interpolated onto a regular  $x$ - $y$  grid after orthorectification and area fractions of ice/melt ponds were  
 558 estimated as a fraction of the total number of pixels for each category (e.g., Fig. A1(d)). The average



fractions of ice/water for a flux period are then calculated by taking an average over all the images in that period. Only flux periods having more than 30 available images are included in the analysis.

## Appendix B: Sensitivity to melt ponds

Here we investigate the sensitivity of our tuning of L2015 to the melt pond fraction. We reclassify 50% and 100% of melt ponds as ice instead of water (Fig. B1) and the L2015 function is re-fitted to the revised ice fractions and compared with our original fit.

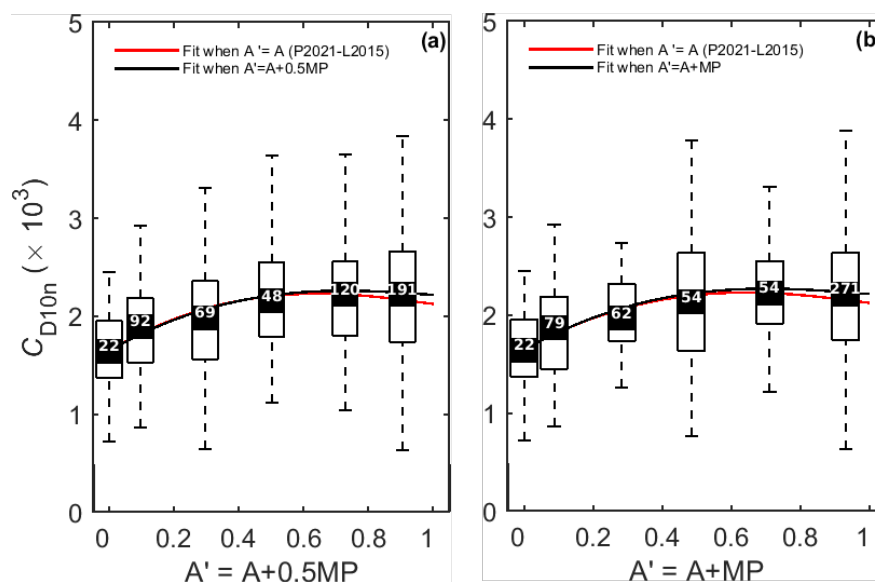


**Figure B1.** Parameterization sensitivity to melt pond fraction (MP). Panel (a) re-classifies half of melt ponds to sea ice ( $A' = A + 0.5 \cdot \text{MP}$ ); while (b) re-classifies all of melt points to sea ice ( $A' = A + \text{MP}$ ), where  $A$  is sea-ice fraction. The curves show the L2015 parameterization, tuned to the original ice fraction observations (red; P2021-L2015) and tuned to the adjusted ice fraction observations (black).

The reclassification of melt ponds as ice has the effect of moving some drag estimates into higher ice fraction bins, slightly increasing the median value of  $C_{D10n}$  at high ice fractions. The refitted L2015 functions reflect this slightly higher drag at high ice fraction but are essentially unchanged for  $A < 0.5$ . Note even when  $A > 0.5$  the change in the L2015 functions is very small compared with the variation in  $C_{D10n}$  within each ice concentration bin. We further investigate the sensitivity of the parameterization to the presence of melt ponds by a simple sub-setting of the data by melt pond fraction. In all cases the melt pond fraction is  $< 0.6$ . Figure B2 shows  $C_{D10n}$  with ice fraction for cases where the melt pond



fraction is  $< 0.3$  (Fig. B2a) and  $< 0.1$  (Fig. B2b). The L2015 function is fit to these subsets of data and compared with that to the full data set. The revised fits differ negligibly from that to the full data set, suggesting that  $C_{D10n}$  is not strongly dependent on the extent of melt ponds. In short, the sensitivity of the parameterization to the treatment of melt ponds is negligible.

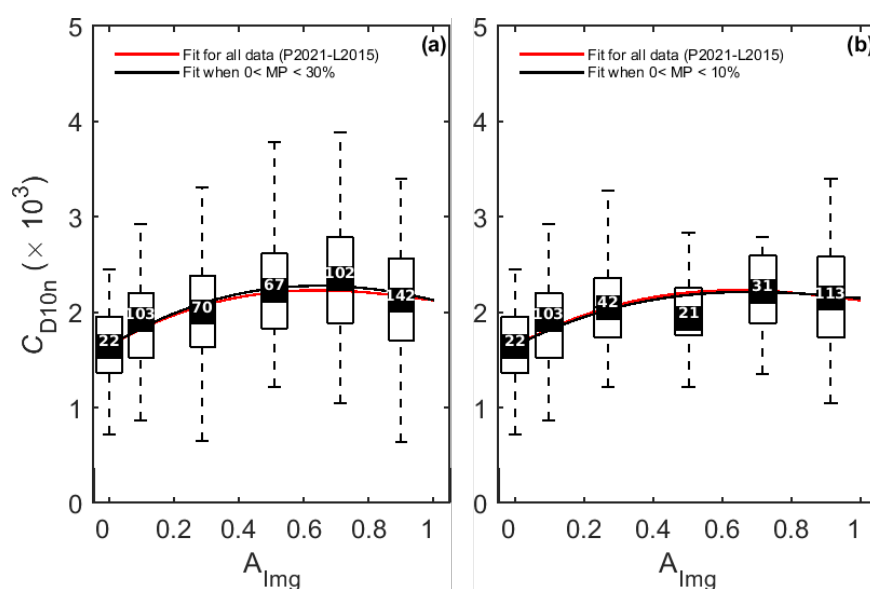


**Figure B2.** (a)  $MP < 30\%$  (b)  $MP < 10\%$ . In each panel, the red curve is the fitting curve obtained for the joint ACSE and AO2016 data same as shown in Figure 8 (P2021-L2015) and the black lines are the fitting curve obtained for the data shown in the ‘respective’ panels.



590 **Data Availability.** The UK ACSE cruise data is publicly available from the Centre for Environmental  
591 Data Analysis (CEDA) archives (<http://archive.ceda.ac.uk>). Data from all participants in both cruises  
592 is publicly available from the Bolin Centre for Climate Research data archive (<https://bolin.su.se/data>).

593 **Author Contributions.** All authors contributed to the design of the study. PS analysed the data sets  
594 and wrote the manuscript with contributions from all co-authors. IMB, JP, and DJS collected the data  
595 during ACSE; IMB and JP collected the data during AO2016. JP processed the flux data. DJS and PS  
596 processed the surface imagery.

597 **Competing interests.** The authors declare no competing interests.

598 **Acknowledgements.** We would like to thank the captains and crews of the icebreaker *Oden*, along with  
599 the technical and logistical support staff of the Swedish Polar Research Secretariat, for their assistance  
600 throughout the ACSE and AO2016 cruises. We thank Michael Tjernström, Ola Persson, Matthew  
601 Shupe, Barbara Brooks, Joseph Sedlar, and Georgia Sotiropoulou for their contributions to the ACSE  
602 measurement campaign.

603 **Financial support.** This work was funded by the UK Natural Environment Research Council (NERC)  
604 grant numbers NE/S000453/1 and NE/S000690/1. MJY was also supported by NERC grant numbers  
605 NE/N018095/1 and NE/V013254/1. The contribution of IMB, JP, and DJS to the ACSE cruise was  
606 funded by NERC grant number NE/K011820/1. Participation in the AO2016 cruise was supported by  
607 the Swedish Polar Research Secretariat.

608

609



## 610 References

- 611 Achtert, P., O'Connor, E., Brooks, I. M., Sotiropoulou, G., Shupe, M. D., Persson, P. O. G., Pospichal,  
 612 B., Brooks, B. J., Tjernström, M.: Properties of Arctic mixed phase clouds from ship-borne  
 613 Cloudnet observations during ACSE 2014, *Atmos. Chem. Phys.* 20, 14983–15002,  
 614 <https://doi.org/10.5194/acp-2020-56>, 2020.
- 615 Arya, S. P. S.: Contribution of form drag on pressure ridges to the air stress on Arctic ice, *J. Geophys.*  
 616 *Res.*, 78, 7092–7099, <https://doi.org/10.1029/JC078i030p07092>, 1973.
- 617 Arya, S. P. S.: A drag partition theory for determining the large-scale roughness parameter and wind  
 618 stress on the Arctic pack ice, *J. Geophys. Res.*, 80, 3447–3454,  
 619 <https://doi.org/10.1029/JC080i024p03447>, 1975.
- 620 Andreas, E. L., Horst, T. W., Grachev, A. A., Persson, P. O. G., Fairall, C. W., Guest, P. S., and Jordan,  
 621 R. E.: Parametrizing turbulent exchange over summer sea ice and the marginal ice zone, *Q. J. Roy.*  
 622 *Meteor. Soc.*, 136, 927–943, <https://doi.org/10.1002/qj.618>, 2010.
- 623 Birnbaum, G. and Lüpkes, C.: A new parameterization of surface drag in the marginal sea ice zone,  
 624 *Tellus* 54A, 107–123, <https://doi.org/10.1034/j.1600-0870.2002.00243.x>, 2002.
- 625 Businger, J. A.: A note on the Businger–Dyer profiles, *Bound.-Lay. Meteorol.*, 42, 145–151,  
 626 [https://doi.org/10.1007/978-94-009-2935-7\\_11](https://doi.org/10.1007/978-94-009-2935-7_11), 1988.
- 627 Castellani, G., Lüpkes, C., Hendricks, S., and Gerdes, R.: Variability of Arctic sea-ice topography and  
 628 its impact on the atmospheric surface drag, *J. Geophys. Res.-Oceans*, 119, 6743–6762,  
 629 doi:10.1002/2013JC009712, 2014.
- 630 Charnock, H.: Wind stress over a water surface, *Q. J. R. Meteorol. Soc.*, 81, 639–  
 631 640, <https://doi.org/10.1002/qj.49708135027>, 1955.
- 632 Ching, J. K.: Ship's influence on wind measurements determined from BOMEX mast and boom data,  
 633 *J. Appl. Meteorol.*, 15(1), 102–106. [https://doi.org/10.1175/1520-0450\(1976\)015%3C0102:SIOWMD%3E2.0.CO;2](https://doi.org/10.1175/1520-0450(1976)015%3C0102:SIOWMD%3E2.0.CO;2), 1976.
- 634 Claussen, M.: Area-averaging of surface fluxes in a neutrally stratified, horizontally inhomogeneous  
 635 atmospheric boundary layer, *Atmos. Environ.*, 24A, 1349–1360, [https://doi.org/10.1016/0960-1686\(90\)90041-K](https://doi.org/10.1016/0960-1686(90)90041-K), 1990.
- 636 Cohen, J., Screen, J. A., Furtado, J. C., Barlow, M., Whittleston, D., Coumou, D., Francis, J., Dethloff,  
 637 K., Entekhabi, D., Overland, J., and Jones, J.: Recent Arctic amplification and extreme mid-latitude  
 638 weather, *Nat. Geosci.*, 7, 627–637, <https://doi.org/10.1038/ngeo2234>, 2014.
- 639 Dai, A., Luo, D., Song, M. and Liu, J.: Arctic amplification is caused by sea-ice loss under increasing  
 640 CO<sub>2</sub>, *Nature Communications*, 10(1), 121, <https://doi.org/10.1038/s41467-018-07954-9>, 2019.
- 641 Drennan, W. M., Graber, H. C., Hauser, D., and Quentin, C.: On the wave age dependence of wind  
 642 stress over pure wind seas, *J. Geophys. Res.*, 108(C3), 8062, doi:10.1029/2000JC000715, 2003
- 643 Edson, J. B., Hinton, A. A., Prada, K. E., Hare, J. E., and Fairall, C. W.: Direct covariance flux  
 644 estimates from mobile platforms at sea, *J. Atmos. Ocean. Tech.*, 15, 547–562,  
 645 [https://doi.org/10.1175/1520-0426\(1998\)0152.0.CO;2](https://doi.org/10.1175/1520-0426(1998)0152.0.CO;2), 1998.
- 646 Elvidge, A. D., Renfrew, I. A., Weiss, A. I., Brooks, I. M., LachlanCope, T. A., and King, J. C.:  
 647 Observations of surface momentum exchange over the marginal ice zone and recommendations for  
 648 its parametrisation, *Atmos. Chem. Phys.*, 16, 1545–1563, [https://doi.org/10.5194/acp-16-1545-](https://doi.org/10.5194/acp-16-1545-2016)  
 649 2016, 2016.
- 650 Elvidge, A. D., Renfrew, I. A., Brooks, I. M., Srivastava, P., Yelland, M. J., Prytherch, J.: Surface heat  
 651 and moisture exchange in the marginal ice zone: Observations and a new parameterization scheme  
 652 for weather and climate models, *J. Geophys. Res.* doi:10.1029/2021JD034827, 2021.
- 653 Foken, T. and Wichura, B.: Tools for quality assessment of surface based flux measurements 1, *Agr.*  
 654 *For. Meteorol.*, 78, 83–105, [https://doi.org/10.1016/0168-1923\(95\)02248-1](https://doi.org/10.1016/0168-1923(95)02248-1), 1996.



- 657 Garbrecht, T., Lüpkes, C., Hartmann, J., and Wolff, M.: Atmospheric drag coefficients over sea ice –  
 658 validation of a parameterisation concept, *Tellus A*, 54, 205–219, [https://doi.org/10.1034/j.1600-](https://doi.org/10.1034/j.1600-0870.2002.01253.x)  
 659 0870.2002.01253.x, 2002.
- 660 Hanssen-Bauer, I. and Gjessing, Y. T.: Observations and model calculations of aerodynamic drag on  
 661 sea ice in the Fram Strait, *Tellus* 40A, 151–161, [https://doi.org/10.1111/j.1600-](https://doi.org/10.1111/j.1600-0870.1988.tb00413.x)  
 662 0870.1988.tb00413.x, 1988.
- 663 Hartmann, J., Kottmeier, C., Wamser, C., and Augstein, E.: Aircraft measured atmospheric  
 664 momentum, heat and radiation fluxes over Arctic sea ice, in: *The polar oceans and their role in*  
 665 *shaping the global environment*, 443–454, <https://doi.org/10.1029/GM085p0443>, 1994.
- 666 Hodson, D. L. R., Keeley, S. P. E., West, A., Ridley, J., Hawkins, E., and Hewitt, H. T.: Identifying  
 667 uncertainties in Arctic climate change projections, *Clim. Dynam.*, 40, 2849–2865,  
 668 <https://doi.org/10.1007/s00382-012-1512-z>, 2013.
- 669 Howes, E. L., Joos, F., Eakin, M., and Gattuso, J.-P.: An updated synthesis of the observed and  
 670 projected impacts of climate change on the chemical, physical and biological processes in the  
 671 oceans, *Front. Mari. Sci.*, 2, 36, <https://doi.org/10.3389/fmars.2015.00036>, 2015.
- 672 Hunke, E. C., and Lipscomb, W. H.: CICE: The Los Alamos sea ice model documentation and software  
 673 user's manual version 4.1. Los Alamos National Laboratory Tech. Rep. LA-CC-06-012, 76 pp.  
 674 [https://csdms.colorado.edu/w/images/CICE\\_documentation\\_and\\_software\\_user's\\_manual.pdf](https://csdms.colorado.edu/w/images/CICE_documentation_and_software_user's_manual.pdf),  
 675 2010.
- 676 Kwok, R.: Arctic Sea ice thickness, volume, and multiyear ice coverage: losses and coupled variability  
 677 (1958–2018). *Env. Res. Letts.*, 13, 105005. <https://doi.org/10.1088/1748-9326/aae3ec>, 2018
- 678 Lehnher, I., St. Louis, V. L., Sharp, M., Gardner, A., Smol, J. P., Schiff, S. L., Muir, D. C. G.,  
 679 Mortimer, C. A., Michelutti, N., Tarnocai, C., St. Pierre, K. A., Emmerton, C. A., Wiklund, J. A.,  
 680 Köck, G., Lamoureux, S. F., and Talbot, C. H.: The world's largest High Arctic lake responds  
 681 rapidly to climate warming. *Nat. Commun.*, 9, 1290, <https://doi.org/10.1038/s41467-018-03685-z>,  
 682 2018.
- 683 LeMone, M.A., Angevine, W.M., Bretherton, C.S., Chen, F., Dudhia, J., Fedorovich, F., Katsaros,  
 684 K.B., Lenschow, D.H., Mahrt, L., Patton, E.G., Sun, J., Tjernström, M., and Weil, J.: 100 Years of  
 685 Progress in Boundary Layer Meteorology. *Meteorological Monographs*, 59, 9.1– 9.85,  
 686 <https://doi.org/10.1175/AMSMONOGRAPH-D-18-0013.1>, 2018.
- 687 Lüpkes, C. and Birnbaum, G.: Surface drag in the Arctic marginal sea-ice zone: A comparison of  
 688 different parameterisation concepts, *Bound.-Lay. Meteorol.*, 117, 179–211,  
 689 <https://doi.org/10.1007/s10546-005-1445-8>, 2005.
- 690 Lüpkes, C., Gryanik, V. M., Hartmann, J., and Andreas, E. L.: A parametrization, based on sea ice  
 691 morphology, of the neutral atmospheric drag coefficients for weather prediction and climate  
 692 models, *J. Geophys. Res.*, 117, D13112, <https://doi.org/10.1029/2012JD017630>, 2012.
- 693 Lüpkes, C., Gryanik, V. M., Rösel, A., Birnbaum, G., and Kaleschke, L.: Effect of sea ice morphology  
 694 during Arctic summer on atmospheric drag coefficients used in climate models, *Geophys. Res.*  
 695 *Lett.*, 40, 446–451, <https://doi.org/10.1002/grl.50081>, 2013.
- 696 Lüpkes, C. and Gryanik, V. M.: A stability-dependent parametrization of transfer coefficients for  
 697 momentum and heat over polar sea ice to be used in climate models, *J. Geophys. Res. Atmos.*, 120,  
 698 552–581, <https://doi.org/10.1002/2014JD022418>, 2015.
- 699 Mai, S., Wamser, C., and Kottmeier, C.: Geometric and aerodynamic roughness of sea ice, *Bound.-*  
 700 *Layer Meteorol.*, 77, 233–248, <https://doi.org/10.1007/BF00123526>, 1996.
- 701 Miao, X., Xie, H., Ackley, S., Perovich, D., and Ke, C.: Object based detection of Arctic sea ice and  
 702 melt ponds using high spatial resolution aerial photographs, *Cold Reg. Sci. Technol.*, 119, 211–222,  
 703 <https://doi.org/10.1016/j.coldregions.2015.06.014>, 2015.
- 704 Moat, B. I., Yelland, M.Y., Brooks, I. M. in NOC Internal Report 17 (National Oceanography Centre,  
 705 2015), <http://eprints.soton.ac.uk/385311/>, 2015.





- Monin, A. S. and Obukhov, A. M.: 1954, ‘Osnovnye zakonomernosti turbulentnogo peremeshivaniya v prizemnom sloe atmosfery (Basic Laws of Turbulent Mixing in the Atmosphere Near the Ground)’, *Trudy geofiz. inst. AN SSSR* 24(151), 163–187
- Notz, D.: Challenges in simulating sea ice in Earth System Models, *Wiley Interdiscip. Rev. Clim. Change*, 3, 509–526, <https://doi.org/10.1002/wcc.189>, 2012.
- Onarheim, I. H., Eldevik, T., Smedsrud, L.H. and Stroeve, J.C.: Seasonal and regional manifestation of Arctic Sea ice loss. *Journal of Climate*, 31, 4917–4932. <https://doi.org/10.1175/JCLI-D-17-0427.1>, 2018.
- Overland, J. E.: Atmospheric boundary-layer structure and drag coefficients over sea ice, *J. Geophys. Res.*, 90(NC5), 9029–9049, <https://doi.org/10.1029/JC090iC05p09029>, 1985.
- Overland, J. E., Dethloff, K., Francis, J. A., Hall, R. J., Hanna, E., Kim, S., Screen, J. A., Shepherd, T. G., and Vihma, T.: Nonlinear response of mid-latitude weather to the changing Arctic, *Nat. Clim. Chang.*, 6, 992–999, <https://doi.org/10.1038/nclimate3121>, 2016.
- Perovich, D. K., Tucker, W. B., and Ligett, K. A.: Aerial observations of the evolution of ice surface conditions during summer, *J. Geophys. Res.*, 107, 8048, <https://doi.org/10.1029/2000JC000449>, 2002.
- Prytherch, J., Yelland, M. J., Brooks, I. M., Tupman, D. J., Pascal, R. W., Moat, B. I., Norris, S. J.: Motion-correlated flow distortion and wave-induced biases in air-sea flux measurements from ships, *Atmos. Chem. Phys.*, 15, 10619–10629, <https://doi.org/10.5194/acp-15-10619-2015>, 2015.
- Prytherch, J., Brooks, I. M., Crill, P. M., Thornton, B. F., Salisbury, D. J., Tjernström, M., Anderson, L. G., Geibel, M. C., and Humborg, C.: Direct determination of the air-sea CO<sub>2</sub> gas transfer velocity in Arctic sea ice regions, *Geophys. Res. Lett.*, 44, <http://doi.org/10.1002/2017GL073593>, 2017.
- Rae, J. G. L., Hewitt, H. T., Keen, A. B., Ridley, J. K., Edwards, J. M., and Harris, C. M.: A sensitivity study of the sea ice simulation in the global coupled climate model, HadGEM3, *Ocean Model.*, 74, 60–76, <https://doi.org/10.1016/j.ocemod.2013.12.003>, 2014.
- Renner, A. H. H., Gerland, S., Haas, C., Spreen, G., Beckers, J. F., Hansen, E., Nicolaus, M., and Goodwin, H.: Evidence of Arctic sea ice thinning from direct observations, *Geophys. Res. Lett.*, 41, 5029–5036, <https://doi.org/10.1002/2014GL060369>, 2014.
- Renfrew, I. A., Elvidge, A. D., and Edwards, J. M.: Atmospheric sensitivity to marginal-ice zone drag: local and global responses. *Q. J. R. Meteorol. Soc.*, 145, 1165–1179, <https://doi.org/10.1002/qj.3486>, 2019
- Ricker, R., Hendricks, S., Kaleschke, L., Tian-Kunze, X., King, J. and Haas, C.: A weekly Arctic sea-ice thickness data record from merged CryoSat-2 and SMOS satellite data. *The Cryosphere*, 11, 1607–1623. <https://doi.org/10.5194/tc-11-1607-2017>, 2017
- Rolph, R. J., Feltham, D. L., and Schröder, D.: Changes of the Arctic marginal ice zone during the satellite era, *The Cryosphere*, 14, 1971–1984, <https://doi.org/10.5194/tc-14-1971-2020>, 2020.
- Roy, F., Chevallier, M., Smith, G., Dupont, F., Garric, G., Lemieux, J.-F., Lu, Y., and Davidson, F.: Arctic sea ice and freshwater sensitivity to the treatment of the atmosphere-ice ocean surface layer, *J. Geophys. Res.-Oceans.*, 120, 4392–4417, <https://doi.org/10.1002/2014JC010677>, 2015.
- Schröder, D., Vihma, T., Kerber, A., and Brümmer, B.: On the parameterisation of Turbulent Surface Fluxes Over Heterogeneous Sea Ice Surfaces, *J. Geophys. Res.*, 108, 3195 <https://doi.org/10.1029/2002JC001385>, 2003.
- Serreze, M. C., and Barry, R. G.: Processes and impacts of Arctic amplification: A research synthesis. *Global and Planetary Change* 77, 490–506, <https://doi.org/10.1016/j.gloplacha.2011.03.004>, 2011
- Sotiropoulou, G., Tjernström, M., Sedlar, J., Achtert, P., Brooks, B. J., Brooks, I. M., Persson, P. O. G., Prytherch, J., Salisbury, D. J., Shupe, M. D. and Johnston, P. E.: Atmospheric Conditions during the Arctic Clouds in Summer Experiment (ACSE): Contrasting Open Water and Sea Ice Surfaces during Melt and Freeze-Up Seasons. *J. Clim.*, 29, 8721–8744, <https://doi.org/10.1175/JCLI-D-16-0211.1>, 2016.



- 755 Spreen, G., Kaleschke, L., and Heygster, G.: Sea ice remote sensing using AMSR-E 89-GHz channels,  
 756 J. Geophys. Res., 113, C02S03, <https://doi.org/10.1029/2005JC003384>, 2008.
- 757 Stössel, A., Cheon, W.-G., and Vihma, T.: Interactive momentum flux forcing over sea ice in a global  
 758 ocean GCM, J. Geophys. Res., 113, C05010, <https://doi.org/10.1029/2007JC004173>, 2008.
- 759 Stroeve, J. C., Kattsov, V., Barrett, A., Serreze, M., Pavlova, T., Holland, M., Meier, W. N.: Trends  
 760 in Arctic sea ice extent from CMIP5, CMIP3 and observations, Geophys. Res. Lett., 39, L16502,  
 761 <https://doi.org/10.1029/2012GL052676>, 2012
- 762 Stroeve, J. C., Hamilton, L., Bitz, C., and Blanchard-Wigglesworth, E.: Predicting September sea ice:  
 763 Ensemble skill of the SEARCH sea ice outlook 2008–2013, Geophys. Res. Lett., 41, 2411–2418,  
 764 <https://doi.org/10.1002/2014GL059388>, 2014.
- 765 Strong, C. and Rigor, I. G.: Arctic marginal ice zone trending wider in summer and narrower in winter,  
 766 Geophys. Res. Lett., 40, 4864–4868, <https://doi.org/10.1002/grl.50928>, 2013.
- 767 Stuecker, M. F., Bitz, C. M., Armour, K. C., Proistosescu, C., Kang, S. M., Xie, S. P., Kim, D.,  
 768 McGregor, S., Zhang, W., Zhao, S., Cai, W., Dong, Y., and Jin, F. F.: Polar amplification dominated  
 769 by local forcing and feedbacks, Nat. Clim. Change, 8, 1076–1081, <https://doi.org/10.1038/s41558-018-0339-y>, 2018.
- 771 Tjernström, M., Shupe, M. D., Brooks, I. M., Persson, P. O. G., Prytherch, J., Salisbury, D. J., Sedlar,  
 772 J., Achtert, P., Brooks, B. J., Johnston, P. E. and Sotiropoulou, G.: Warm-air advection, air mass  
 773 transformation and fog causes rapid ice melt, Geophys. Res. Lett., 42, 5594–5602,  
 774 <https://doi.org/10.1002/2015GL064373>, 2015.
- 775 Tjernström, M., Shupe, M. D., Prytherch, J., Achtert, P., Brooks, I. M., and Sedlar, J.: Arctic summer  
 776 air-mass transformation, surface inversions and the surface energy budget, J. Clim., 32, 769–789,  
 777 <https://doi.org/10.1175/JCLI-D-18-0216.1>, 2019.
- 778 Tsamados, M., Feltham, D. L., Schroeder, D., Flocco, D., Farrell, S. L., Kurtz, N., Laxon, S. L., and  
 779 Bacon, S.: Impact of Variable Atmospheric and Oceanic Form Drag on Simulations of Arctic Sea  
 780 Ice, J. Phys. Oceanogr., 44, 1329–1353, <https://doi.org/10.1175/JPO-D-13-0215.1>, 2014.
- 781 Vihma, T.: Subgrid Parameterization of Surface Heat and Momentum Fluxes over Polar Oceans, J.  
 782 Geophys. Res., 100, 22625–22646, <https://doi.org/10.1029/95JC02498>, 1995.
- 783 Vihma, T., Pirazzini, R., Fer, I., Renfrew, I. A., Sedlar, J., Tjernström, M., Lüpkes, C., Nygård, T.,  
 784 Notz, D., Weiss, J., Marsan, D., Cheng, B., Birnbaum, G., Gerland, S., Chechin, D., and Gascard,  
 785 J. C.: Advances in understanding and parameterization of small-scale physical processes in the  
 786 marine Arctic climate system: a review, Atmos. Chem. Phys., 14, 9403–9450, doi:10.5194/acp-14-  
 787 9403-2014, 2014.
- 788 Webster, M. A., Rigor, I. G., Perovich, D. K., Richter-menge, J. A., Polashenski, C. M., and Light, B.:  
 789 Seasonal evolution of melt ponds on Arctic sea ice, J. Geophys. Res., 120, 5968–5982,  
 790 <https://doi.org/10.1002/2015JC011030>, 2015.
- 791 Weissling, B., Ackley, S., Wagner, P., Xie, H.: EISCAM — Digital image acquisition and processing  
 792 for sea ice parameters from ships, Cold Reg. Sci. Technol., 57, 49–60,  
 793 doi:10.1016/j.coldregions.2009.01.001, 2009
- 794 Wright, N. C. and Polashenski, C. M.: Open-source algorithm for detecting sea ice surface features in  
 795 high-resolution optical imagery, The Cryosphere, 12, 1307–1329, <https://doi.org/10.5194/tc-12-1307-2018>, 2018.
- 797 Yelland, M. J., Moat, B. I., Pascal, R. W., and Berry, D. I.: CFD model estimates of the airflow  
 798 distortion over research ships and the impact on momentum flux measurements. J. Atmos. Ocean  
 799 Tech., 19(10), 1477–1499, [https://doi.org/10.1175/1520-0426\(2002\)019<1477:CMEOTA>2.0.CO;2](https://doi.org/10.1175/1520-0426(2002)019<1477:CMEOTA>2.0.CO;2), 2002.
- 801 Yelland, M. J., Moat, B. I., Taylor, P. K., Pascal, R. W., Hutchings, J., and Cornell, V. C.: Wind stress  
 802 measurements from the open ocean corrected for airflow distortion by the ship. J. Phys. Ocean.,  
 803 28(7), 1511–1526., [https://doi.org/10.1175/1520-0485\(1998\)028<1511:WSMFTO>2.0.CO;2](https://doi.org/10.1175/1520-0485(1998)028<1511:WSMFTO>2.0.CO;2), 1988





804 Zampieri, L., Goessling, H. F., and Jung, T.: Bright prospects for Arctic sea ice prediction on  
805 subseasonal time scales, *Geophys. Res. Letts.*, 45, 9731–9738,  
806 <https://doi.org/10.1029/2018GL079394>, 2018.